AGU PUBLICATIONS

Geochemistry, Geophysics, Geosystems

RESEARCH ARTICLE
10.1002/2016GC006338

Special Section:
Magnetism From Atomic to Planetary Scales: Physical Principles and Interdisciplinary Applications in Geo- and Planetary Sciences

Shock-induced deformation phenomena in magnetite and their consequences on magnetic properties

Boris Reznik[1], Agnes Kontny[1], Jörg Fritz[2], and Uta Gerhards[3]

[1]Karlsruhe Institute of Technology, Institute of Applied Geosciences, Karlsruhe, Germany, [2]Saalbau Weltraum Projekt, Heppenheim, Germany, [3]Karlsruhe Institute of Technology, Institute for Micro Process Engineering, Eggenstein-Leopoldshafen, Germany

Abstract This study investigates the effects of shock waves on magnetic and microstructural behavior of multidomain magnetite from a magnetite-bearing ore, experimentally shocked to pressures of 5, 10, 20, and 30 GPa. Changes in apparent crystallite size and lattice parameter were determined by X-ray diffraction, and grain fragmentation and defect accumulation were studied by scanning and transmission electron microscopy. Magnetic properties were characterized by low-temperature saturation isothermal remanent magnetization (SIRM), susceptibility measurements around the Verwey transition as well as by hysteresis parameters at room temperature. It is established that the shock-induced refinement of magnetic domains from MD to SD-PSD range is a result of cooperative processes including brittle fragmentation of magnetite grains, plastic deformation with shear bands and twins as well as structural disordering in form of molten grains and amorphous nanoclusters. Up to 10 GPa, a decrease of coherent crystallite size, lattice parameter, saturation magnetization (*Ms*), and magnetic susceptibility and an increase in coercivity, SIRM, and width of Verwey transition are mostly associated with brittle grain fragmentation. Starting from 20 GPa, a slight recovery is documented in all magnetic and nonmagnetic parameters. In particular, the recovery in SIRM is correlated with an increase of the lattice constant. The recovery effect is associated with the increasing influence of shock heating/annealing at high shock pressures. The strong decrease of *Ms* at 30 GPa is interpreted as a result of strong lattice damage and distortion. Our results unravel the microstructural mechanisms behind the loss of magnetization and the modification of magnetic properties of magnetite and contribute to our understanding of shock-induced magnetic phenomena in impacted rocks on earth and in meteorites.

Key Points:
- The effect of shock waves on microstructure and magnetic properties of magnetite is studied
- Our results unravel the microstructural mechanisms behind the loss of magnetization and the modification of magnetic properties
- Our approach can be applied for studies aiming to understand the shock-induced magnetic phenomena in rocks on earth and in meteorites

Correspondence to:
B. Reznik,
boris.reznik@kit.edu

Citation:
Reznik, B., A. Kontny, J. Fritz, and U. Gerhards (2016), Shock-induced deformation phenomena in magnetite and their consequences on magnetic properties, *Geochem. Geophys. Geosyst.*, *17*, 2374–2393, doi:10.1002/2016GC006338.

Received 2 MAR 2016
Accepted 23 MAY 2016
Accepted article online 27 MAY 2016
Published online 24 JUN 2016

1. Introduction

Magnetite and pyrrhotite are the most important magnetic minerals in impacted terrestrial rocks and play also a significant role in other solar system bodies, which are mostly assumed to have suffered some degree of shock pressure. Prominent examples are the Martian meteorites. Magnetic carriers in those meteorites are magnetite, pyrrhotite, and titanomagnetite [e.g., *Rochette et al*., 2001; *Louzada et al*., 2011]. Shock waves permanently modify the intrinsic magnetic properties of rocks, and these changes are attributed to fracturing and/or plastic deformation phenomena in the magnetic minerals [e.g., *Gilder et al*., 2004; *Gattacceca et al*., 2007; *Louzada et al*., 2010; *Mang et al*., 2013]. Static pressure experiments have consistently documented that all magnetic minerals substantially demagnetize at pressures of a few GPa and that the degree of demagnetization depends strongly on magnetic mineralogy and magnetic domain state [*Gilder et al*., 2004; *Bezaeva et al*., 2007; *Louzada et al*., 2011]. In an ambient magnetic field, rocks with ferromagnetic, minerals can acquire a shock remanent magnetization (SRM) during the passage of a shock wave, which can persist to unblocking temperatures near the Curie point [e.g., *Tikoo et al*., 2015, and references therein].

Effects of shock waves on the intrinsic magnetic properties of magnetite are still poorly understood, especially concerning the correlation between shock-induced magnetic and microstructural properties. Shock recovery experiments on magnetite-bearing alumina powder pellets between 10 and 45 GPa revealed an overall magnetic softening of magnetic properties [*Kohout et al*., 2012]. These results are representative for impacts into highly porous, magnetite-bearing sedimentary or volcanic rocks but are in contrast to all other studies to date [e.g., *Pesonen et al*., 1997; *Gilder et al*., 2002; *Gattacceca et al*., 2007]. *Gattacceca et al*. [2007] investigated the effects of explosive-driven shock on the magnetic properties of magnetite-bearing

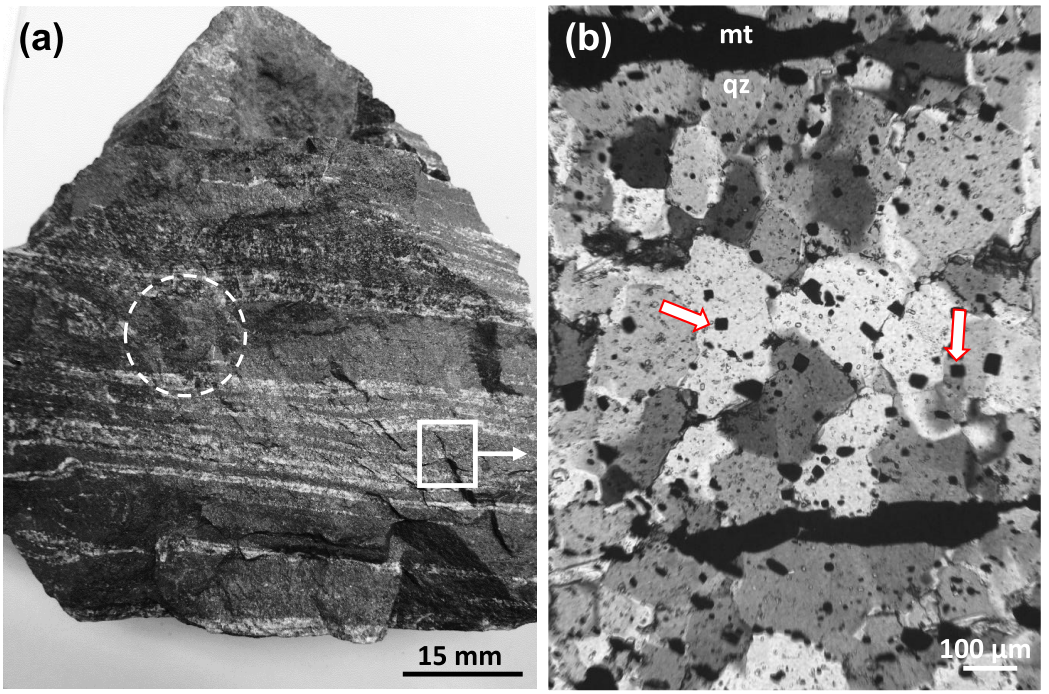

Figure 1. Target material. (a) Hand specimen of the banded magnetite-quartz ore. Dark bands are magnetite rich, while the light bands contain more quartz. Dashed circle illustrates that disks for the shock experiments were prepared from the magnetite-rich bands. (b) Transmitted light microscope image of a light band with magnetite (mt) appearing in form of polycrystalline strings and single grains embedded in a quartz (qz) matrix. Arrows mark mt-grains with cubic shapes.

quartzitic microdolerite. For pressures up to about 10 GPa, a noticeable decrease of coercivity and a slight increase of specific magnetic susceptibility were found. Only for highly shocked samples up to 30 GPa, a slight decrease of specific magnetic susceptibility was observed in agreement with earlier studies of *Hargraves and Perkins* [1969]. Although variations in magnetic properties were attributed to fracturing and/or dislocations of the ferrimagnetic grains, detailed microstructural studies were not carried out in these studies.

Our study addresses the effect of shock pressures between 5 and 30 GPa on mineralogical, microstructural, and magnetic properties of magnetite after decompression and therefore is a good analogue for magnetite-bearing impact rocks from Earth and meteorites. Our results shed light on shock deformation phenomena and their influence on the intrinsic magnetic properties of magnetite. We found that a combination of grain fracturing, plastic deformation mechanisms, and amorphization are the main phenomena influencing coercivity, magnetic memory, and Verwey transition temperature in magnetite.

2. Materials and Methods

2.1. Target Material

This study uses a metamorphic quartz-magnetite banded iron ore from the Sydvaranger mine, Finnmark/Norway. Microscopically, the ore is characterized by layers of polycrystalline quartz with equilibrated grain boundaries and cubic magnetite crystals disseminated in the quartz matrix and polycrystalline magnetite forming strings parallel to the banding (Figure 1). The sharp Verwey transition at $-152°C \pm 2°C$ as well as a clearly defined Curie temperature at $578 \pm 2°C$ attest a relatively high purity of magnetite. Crushing, screening, and magnetic separation steps were applied to determine the weight percentage of bulk magnetic and nonmagnetic ore components. To obtain a representative modal composition, an ore piece of about 50 g was used. After few repetitions of the separation steps and control by optical microscopy, batches of well-isolated magnetic and nonmagnetic ore components were obtained. The weight component of magnetite determined in this way was ~80%, which allowed to obtain representative results for all studied shocked samples. The 20% of nonmagnetic component consists of about 18% quartz and 2% subordinate and

Table 1. Conditions for Shock Experiments

Sample Thickness (mm)	Pressure P (GPa)	Cover Plate Thickness (mm)	Flyer Plate Thickness (mm)	Acceleration Tool	Initial Pressure Iron (GPa)	Velocity of Flyer Plate v (km/s)	Shock Duration (μs)
1.28	5	2	5	Air gun	7	0.35	1.8
1.31	10	17.5	4	TNT, explosives	30	1.55	0.6
1.28	20	17.5	4	Comp. B (64), explosives	42	1.99	0.4
1.29	30	13	4	Comp. B (64), explosives	42	1.99	0.5

accessory components represented by amphibole, chlorite, biotite, and pyrite. As it is illustrated by the dashed circle in Figure 1a, disks of 15 mm diameter were cut from the magnetite-rich bands containing about 88% of magnetite. The prepared pore-free rigid disks were an appropriate material for the efficient energy transfer of shock waves.

2.2. Shock Recovery Experiments

Shock recovery experiments were conducted at the Ernst Mach institute, Freiburg, Germany, using the shock reverberation setup described in detail elsewhere [*Muller and Hornemann*, 1969; *Fritz et al*., 2011]. A flyer plate was accelerated with either an air gun or high explosives to a given velocity. The flyer plate impacts an ARMCO iron container containing the disk-shaped target. By a series of shock reverberations, the well-defined shock conditions in the high impedance ARMCO iron container are enforced onto the magnetite target. The preset shock pressure values were calculated using the Hugoniot data for iron [*Muller and Hornemann*, 1969] and magnetite [*RusBank*; *Marsh*, 1980]. Applying of rather thick sample sizes (∼1.3 mm, see Table 1) provides conditions for two shock reflections. This allow to subject well-defined shock pressures distributed homogeneously within the target volume (Table 1).

Using a digital GMH 3710 thermometer (accuracy ∼0.1°C), we estimated the cooling rate of the iron containers to ambient temperatures after shock experiments with 20 and 30 GPa. Five minutes after the shock, the postshock temperature of the containers was 95°C and cooled in a rate of 1°C/min. We were not able to measure the peak shock temperature of the containers in the previous 5 min, because the samples had to be taken out of the explosion chamber, which was only possible after a few minutes.

After the shock experiments, the disks were divided in cake-like pieces and either tiny shocked magnetite pieces were used for SEM, TEM, low-temperature magnetometry, and hysteresis measurements or small amounts were gently pulverized and used for X-ray powder diffraction or temperature-dependent magnetic susceptibility measurements.

2.3. X-ray Powder Diffraction

X-ray powder diffraction (Kristalloflex D500, Siemens) was carried out using a copper tube and graphite monochromator. For each sample, the 2θ range 10–63° was scanned with an angular speed of 0.5°/min. To determine the instrumental broadening function and the exact Bragg positioning of the magnetite peaks, Si and CaWO4 powders were used as standard materials. The average lattice parameter *a*, was calculated from shifts of Kα1 lines of (511) and (440) peaks.

For the estimation of the average crystallite size, the observed spectra were separated into two peaks originated from *K*α1 and *K*α2 lines of Cu target, by a procedure described by *Alexander and Klug* [1950].

Diffraction peaks can be broadened by reduction in grain size below 200 nm or by introducing strain into the crystal lattice. Therefore, we used in addition to the Scherrer equation, which takes only grain size reduction into account, the Williamson-Hall (W-H) technique, which also calculates strain [*Williamson and Hall*, 1953]. According to the W-H technique, the total X-ray peak broadening is caused by a reduction in the apparent crystallite size and/or internal strain. The following expression is used to extract crystallite and strain components:

$$\beta \cos \theta = 0.9\lambda/D_{WH} + 4\varepsilon \sin \theta \quad (1)$$

where β is the FWHM of the Bragg peaks (in radians), θ is the Bragg angle of the analyzed peak, and λ is the wavelength of the X-ray ($\lambda_1 = 0.154056$ nm for Cu-*K*α1), D_{WH} is the average crystallite size, and ε is the strain. The resulting plot is a straight line from which intercept with *y* axis, slope D and ε are determined. Equation (1) assumes that the strain is uniform in all crystallographic directions, which is known as the uniform

deformation model (UDM). In this model, the crystal is considered as isotropic in nature, and it is assumed that the properties of the material are independent of the direction along which it is measured [*Williamson and Hall*, 1953; *Langenhorst*, 1994].

Additionally, the apparent crystallite size was estimated from the full width at half maximum (FWHM) of the X-ray diffraction peak using Scherrer's equation:

$$D = K\lambda/(\beta \cos \theta), \quad (2)$$

where D is the crystal diameter, λ the X-ray wavelength, β the FWHM of a diffraction peak, (311) in our case, θ is the diffraction angle, and K is the Scherrer's constant in the order of unity for usual crystals.

2.4. Scanning Electron Microscopy

The shock-induced fracture morphology was investigated by high-resolution scanning electron microscopy (HRSEM) using a LEO Gemini 1530 microscope operated at 10 kV. A magnetized steel pin was used to extract a tiny magnetic fraction from the powdered samples. The samples were transferred to the SEM on a double-sided conductive adhesive tab mounted on an aluminum holder. Prior to the examinations the sample was coated with a 5 nm thick Pt-Pd conductive layer. During the SEM observations, the chemical composition of the grains was controlled using energy-dispersive X-ray analyzer (Thermo Scientific).

2.5. Electron Probe Microanalysis

Additionally, the chemical composition of magnetite grains was analyzed with a Jeol JXA-8530F electron-microprobe using accelerating voltage of 15 kV and a probe current of 20 nA. Magnetite grains from polished thin sections were compared with polished samples of synthetic magnetite from Merck, Germany, and pure iron, which were used as standards. In all studied samples (about 10 measurements per grain), no detectable signals of possible impurities like Ti, Cr, V, Al, Mg, or Mn were found during electron microprobe analyses. Furthermore, the stoichiometric ratio of Fe and O measured in unshocked and shocked samples corresponds to those of pure magnetite.

2.6. Transmission Electron Microscopy

TEM investigations aimed to follow the evolution of shock-induced lattice defects at the atomic level. In magnetite, the plastic deformation and the accompanying defects can develop by movements along the {111} planes in the <110> direction. To study defect formation in different shocked sample under the same crystallographic conditions, thin lamellae for TEM observations were cut with a focused iron beam (FIB) along the <110>-orientation as it is shown in Figure 2. Magnetite grains exhibiting nearly cubic shape could be selected following SEM observations, since such grains are frequently observed in this ore (Figure 1).

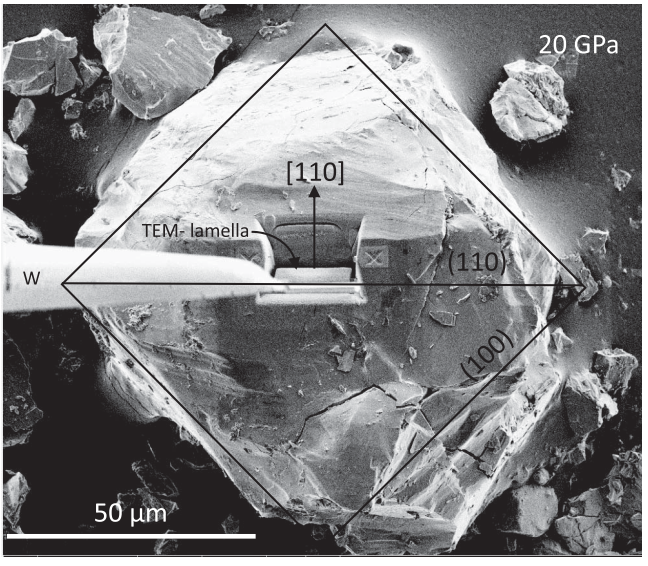

Figure 2. SEM image illustrating the target for focused ion beam (FIB) preparation of TEM lamellae as detailed in the text. The SEM image shows a top-down view of a cubic-shaped magnetite grain after milling of trenches along the diagonal (110) plane. The TEM lamella is mounted to the W-wire of a nanomanipulator.

The TEM lamellae were prepared with a FIB milling station FEI Dual Beam Strata 400S using a Ga+ cathode. Here the area of interest was coated with a 3 μm thick conductive platinum layer. The sample was cut from the thin-sections by a 30kV, 6.5 nA Ga ion beam and thinned by a 30 kV, 26 pA Ga ion beam. Two to three, 5–50 nm thick windows were prepared to check for FIB-induced damage and amorphization. In the final step, the sample was polished and cleaned with a 5 kV (71 pA) ion current. This step is essential to remove its crust, which is commonly damaged by the high-energy ion beam.

The TEM investigations were carried out with a Philips CM 200 FEG/ST TEM operated at 200 kV. We avoided sample amorphization by using a sample holder cooled with liquid nitrogen, and a short exposure time of about 10–20 ms. A condenser aperture of 100 μm at a spot size of ≥300 nm was used for the initial selective area electron diffraction (SAED) images and general TEM investigations. Usually much higher energy is transmitted to the sample during high-resolution TEM (HRTEM) investigations. For the HRTEM investigations, the beam was first focused at a location away from the area of interest and only then the investigations were carried out.

2.7. Magnetic Measurements

For the magnetic measurements we used either small pieces of magnetite or the same pulverized shock sample, which were used for the X-ray analysis. Three to five different portions from each shock experiment were used for different magnetic techniques.

Susceptibility measurements around the Verwey transition were made at the Karlsruhe Institute for Technology (KIT, Karlsruhe, Germany) using an AGICO KLY-4S Kappabridge (effective field intensity: 300 A/m; frequency: = 875 Hz) with a CS-L low-temperature (from 83 to 300 K) attachment. According to the manufacturer of the thermometer (JUMO), the recorded temperature values are accurate within ±1 K. Transition temperatures were calculated from the maximum in the first derivative curves.

Furthermore, at the Institute for Rock Magnetism (IRM, Minneapolis), saturation isothermal remanent magnetization (SIRM) behavior, hysteresis parameters, and first-order reversal curve (FORC) distributions were analyzed. SIRM was produced in a magnetic field of 2.5 T at 300 K using a MPMS 2 SQUID magnetometer and then studied around the Verwey transition. The hysteresis measurements at room temperature were conducted on a Princeton Measurements vibrating sample magnetometer exhibiting a sensitivity of 5×10^{-9} A/m^2. From the hysteresis measurements, the values of remanent magnetization after saturation *Mrs*, saturation magnetization *Ms*, coercivity *Hc*, and coercivity of remanence *Hcr* were extracted. To classify magnetic domain states, the ratios of the hysteresis parameters (*Mrs*/*Ms* versus *Hcr*/*Hc*) were presented as Day plot [*Day et al*., 1977]. A refinement of the Day plot was made using the calculated values for multidomain (MD), single-domain (SD), and pseudosingle-domain (PSD) mixtures [*Dunlop*, 2002]. FORC diagrams were calculated from major hysteresis loops using FORCinel software [*Harrison and Feinberg*, 2008].

3. Results

3.1. X-Ray Powder Diffraction

The results of the X-ray diffraction analysis are shown in Figure 3. For the initial sample, sharp Fe_3O_4 peaks with no measurable contributions from maghemite or hematite occur (Figure 3a, black curve). The intensity and Bragg positions of the diffraction peaks were consistent with the standard pattern for synthetic magnetite (JCPDS Card No. 79–0417, lattice constant $a_0 = 8.394$ Å) and are in a good accordance with the electron-microprobe measurements (see section 2.5) indicating a high chemical purity of magnetite.

The diffraction profiles of the shocked samples contain the same set of magnetite peaks as the unshocked magnetite (Figure 3a). This fact suggests that the applied shock pressures did not provoke a measurable amount of phase transformations in magnetite. A closer look at the profiles reveals that increasing shock pressure correlates with asymmetric broadening of the diffraction peaks and decreasing of its Bragg positions, seen in the evolution of the (511) peak in Figure 3b. Simultaneously, a prominent broadening and shift of the quartz (21-1) peak can be recognized (Figure 3b). Physical broadening of magnetite reflections was used to construct Williamson-Hall plots (Figure 3c). Generally, compared to the initial sample, the Williamson-Hall plots from the shocked samples are shifted toward increasing $\beta\cos\theta$ values. This fact suggests that the increasing shock pressure correlates with the decreasing size of apparent crystallite sizes. The Williamson-Hall plot of the initial sample can be roughly approximated by a straight line which slope indicates the presence of internal strains. However, the Williamson-Hall plots from the shocked samples cannot be definitely approximated by straight lines allowing to determine realistic values of apparent crystallite sizes and strains. With other words, the scattered data from the shocked samples (Figure 3c) do not obey the UDM formulation assuming an isotropic distribution of internal stresses [*Williamson and Hall*, 1953; *Prabhu and Rao*, 2014] but indicate that the shock-induced strain is anisotropic, i.e. are strongly dependent from crystallographic direction.

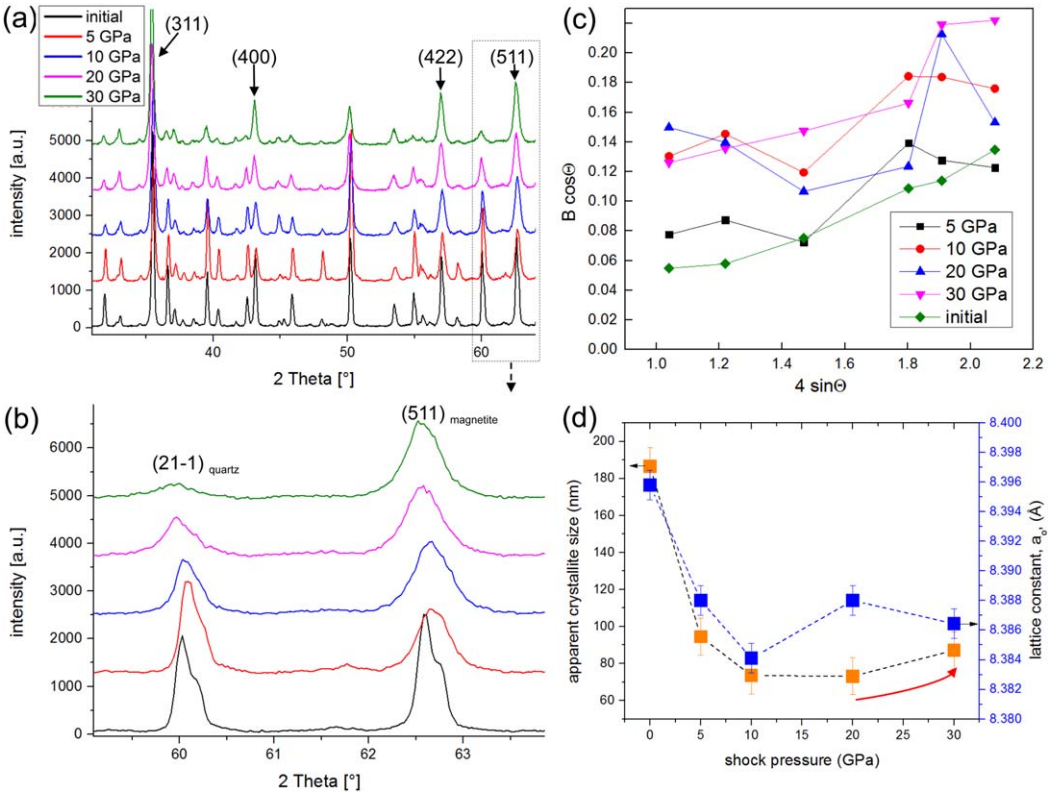

Figure 3. Effect of shock pressure on the evolution of X-ray powder diffraction profiles. (a) Overview patterns containing numerous diffraction peaks of quartz and magnetite. The (hkl) indexing is only given for the magnetite peaks. (b) Magnified high-angle diffraction area from Figure 3a (the area labeled by the dashed rectangle in Figure 3a) shows prominent broadening and shift of (21-1) quartz and (511) magnetite peaks. (c) Williamson-Hall plots indicate a complex and nonlinear relationship between broadening of X-ray peaks and increasing shock pressure. (d) Estimated apparent crystallite size and lattice constant, a_o, as a function of shock pressure. Note that both values drop sharply from 0 to 10 GPa and are less diminished (red arrows) above 20 GPa.

The relationship between shock pressure and average crystal size extracted from the (311) peak broadening using Scherrer equation (2) and lattice parameter a_o extracted from (511) and (440) peak shifts are shown in Figure 3d. Both relationships indicate two prominent pressure regimes. Up to 10 GPa, the average crystal size and lattice parameter decrease while at 20 and/or 30 GPa the difference between initial and shocked sample is less pronounced.

3.2. Scanning Electron Microscopy

SEM observations of shock-generated fracture morphology are presented in Figure 4. Magnetite grains with well-developed cubic smooth {001} faces can be observed. In the crushed unshocked samples (Figure 4a), intergranular fractures follow the boundaries between quartz and magnetite grains. The magnetite crystal faces show no deformation except cracks propagating parallel to crystallographic planes (Figure 4b). On the contrary, the shocked samples are characterized by intensive grain fragmentation accompanied by the development of various types of defects with increasing shock pressure. Intercrossing microshear bands appear in all shocked magnetite samples. Figures 4c and 4d show shear bands lying within the crystal faces, which are characterized by shifted terraces in the 10 GPa sample. Starting at 20 GPa (Figure 4e) we observed nanosized globular grains along sheared terraces. This observation indicates local overheating that can lead to localized melting or amorphization. A further increase in shock pressure to 30 GPa is characterized by the formation of twin-like lamellae (Figure 4f).

3.3. Transmission Electron Microscopy

Deformation microstructures in magnetite were investigated in details by TEM (Figures 5–7). The low-resolution images (Figure 5) show that all shocked samples are characterized by the development of microshear bands (see arrows) that form boundaries between lamellar subgrains of alternating image contrast.

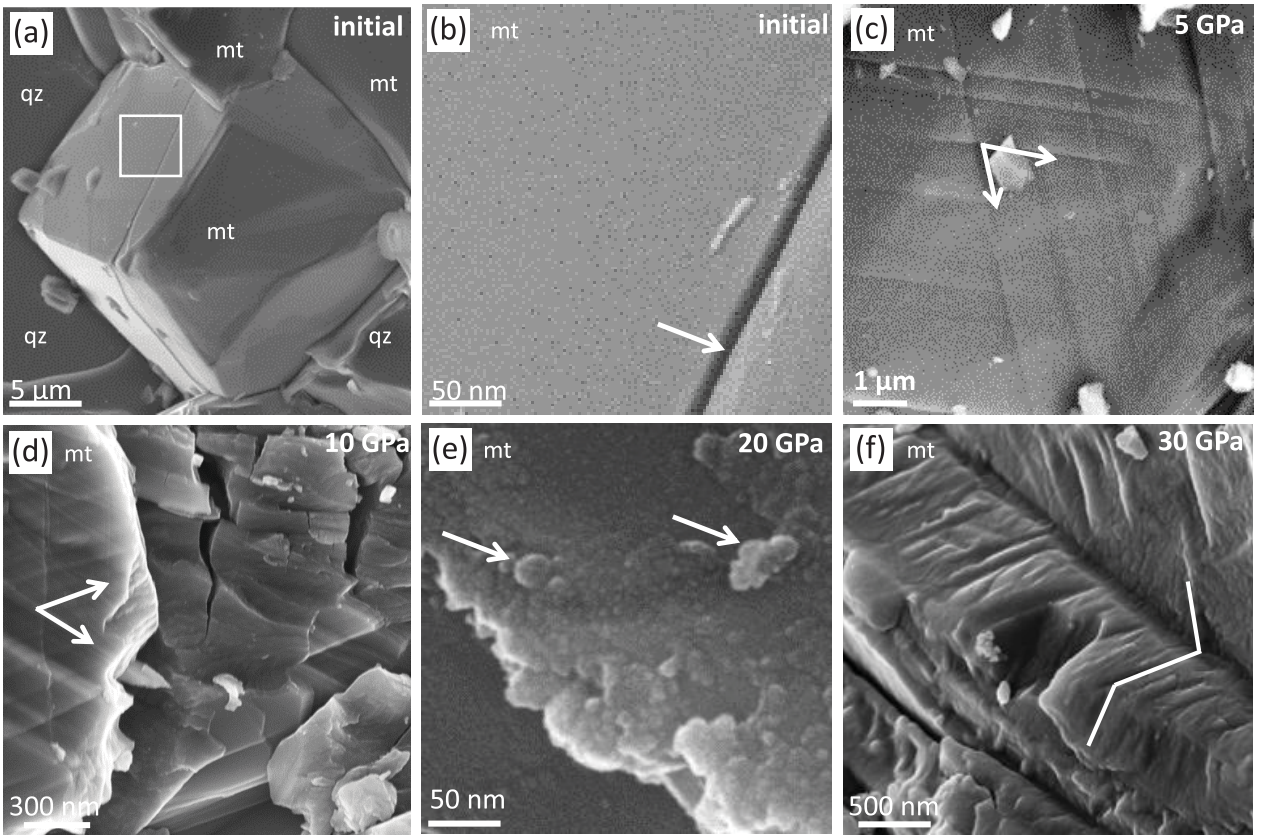

Figure 4. SEM observations of fracture morphology. (a, b) Manually fractured unshocked sample composed of quartz (qz) and magnetite (mt) grains. Note the well-developed cubic smooth faces shown in Figure 4b, which corresponds to the area labeled by the white frame in Figure 4a. The arrow in Figure 4b points on a crack propagating parallel to the {001} plane. (c) Shear bands (arrows) in the 5 GPa sample. (d) Particle fragmentation with shear bands indicated by arrows in the 10 GPa sample. (e) Globular nanograins indicated by arrows on shear terraces in the 20 GPa sample. (f) Twin-shaped lamellae in the 30 GPa sample.

The detailed nanostructure around shear bands was studied using high-resolution imaging (Figures 6 and 7). Shear bands with different periods/widths can be recognized in the 10 GPa sample (Figure 6a). The boundaries of the bands can be approximately associated with elongated dark regions. The total thickness of a large band is about 20 nm that roughly corresponds to the thickness of the white band highlighted by the arrow in Figure 5b. Within the large band, smaller 6 nm thick periodic bands are running parallel to the [−11 −1] direction (Figure 6a). Higher magnification of an area at the band boundary (Figure 6b) reveals discontinuous lattice fringes that are located in dark amorphous-like regions indicated by circles, as well as zig-zag shaped areas with twin-like boundaries as indicated by white curved lines in Figure 6b. Similar but more developed shear bands and amorphous-like mosaic subgrains are typical for samples shocked to 20 GPa (Figures 6c and 6d). In this case, the total thickness of the large shear band is about 50 nm while the smaller periodic bands are 15 nm thick (Figure 6c). Compared to the sample shocked at 10 GPa (Figure 6b), the 20 GPa sample shows the zig-zag shaped regions with a higher contrast between crystalline and disordered, amorphous regions (Figure 6d). Next to the sharper twin-like boundaries separating domains of approximately 2 × 5 nm in size (see the marked boundaries at the right side) the zig-zag shaped structures can be clearly recognized (Figure 6d).

More drastic structural changes occur in magnetite shocked to 30 GPa. Figure 7 shows ∼12 nm thick lamellae composed of two families of twins. In Figure 7a, the primary twin family corresponds to two matrix elements labeled by boxes (b) and (d) and to a twinned element marked by the box (c). The corresponding FFT diffractograms (Figures 7b–7d) demonstrate that the twin subgrain (c) is rotated by 70° in relation to the matrix subgrains (b) and (d). The secondary twin family corresponds to the numerous nanotwins occurring in a transitional area between the matrix and a twinned subgrain (Figure 7e). The nanostructure of a shear band formed at 30 GPa can be described as a kink-band (Figure 7f), which is a result of plastic

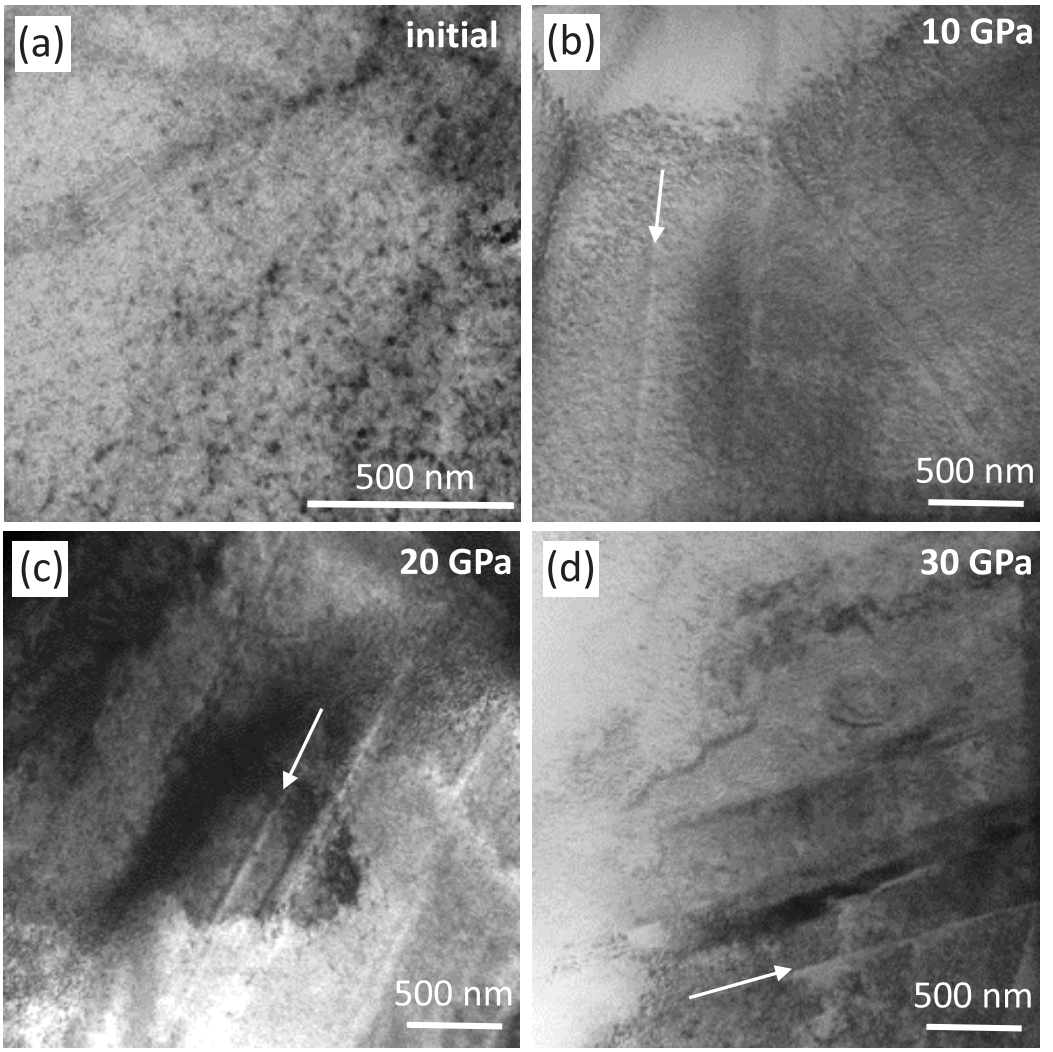

Figure 5. TEM bright-field micrographs of selected magnetite thin sections. Note that compared to the initial, (a) preshock sample, the shocked samples contain planar deformation bands (arrows) between lamellar subgrains. In all images, the samples are oriented with their [110] axis parallel to the incident electron beam.

buckling occurring at the highest shock pressure applied in this study. Note that similar kinked structures are also observed in this sample by SEM (Figure 4d).

3.4. Hysteresis Parameters

Complementary to the microstructural shock-induced changes, variations in magnetic properties were also determined. Hysteresis parameters are presented in Table 2.

The remanence ratio *Mrs/Ms* increases continuously up to 10 GPa and then remains nearly unchanged (Table 2). The *Hcr/Hc* ratio decreases abruptly in the 5 GPa and then increases slightly up to 30 GPa (Table 2). Figure 8 is a Day-Dunlop plot showing the effect of shock pressure on the hysteresis parameter ratios and the magnetic domain state. The remanence ratios *Mrs/Ms* of 0.02 and *Hcr/Hc* of 5.8 indicate that magnetite in the initial, unshocked sample is in the multidomain state. The shocked magnetite displays hysteresis ratios, which correspond to the pseudo-single-domain field. As a general trend, the hysteresis ratios indicate a reduction of magnetic domain size with increasing shock pressure. The strongest changes occur again up to 10 GPa while at higher shock pressures only small further changes occur and a weak evolution toward a higher percentage of MD grains, called as recovery effect, was observed. The percentage of MD grains is about 72% at 5 GPa and then decreases to 63% at 10 GPa, and recovers very slightly to about 65% at 20 and 30 GPa, respectively (see segmented line in Figure 8). Note that the hysteresis parameters

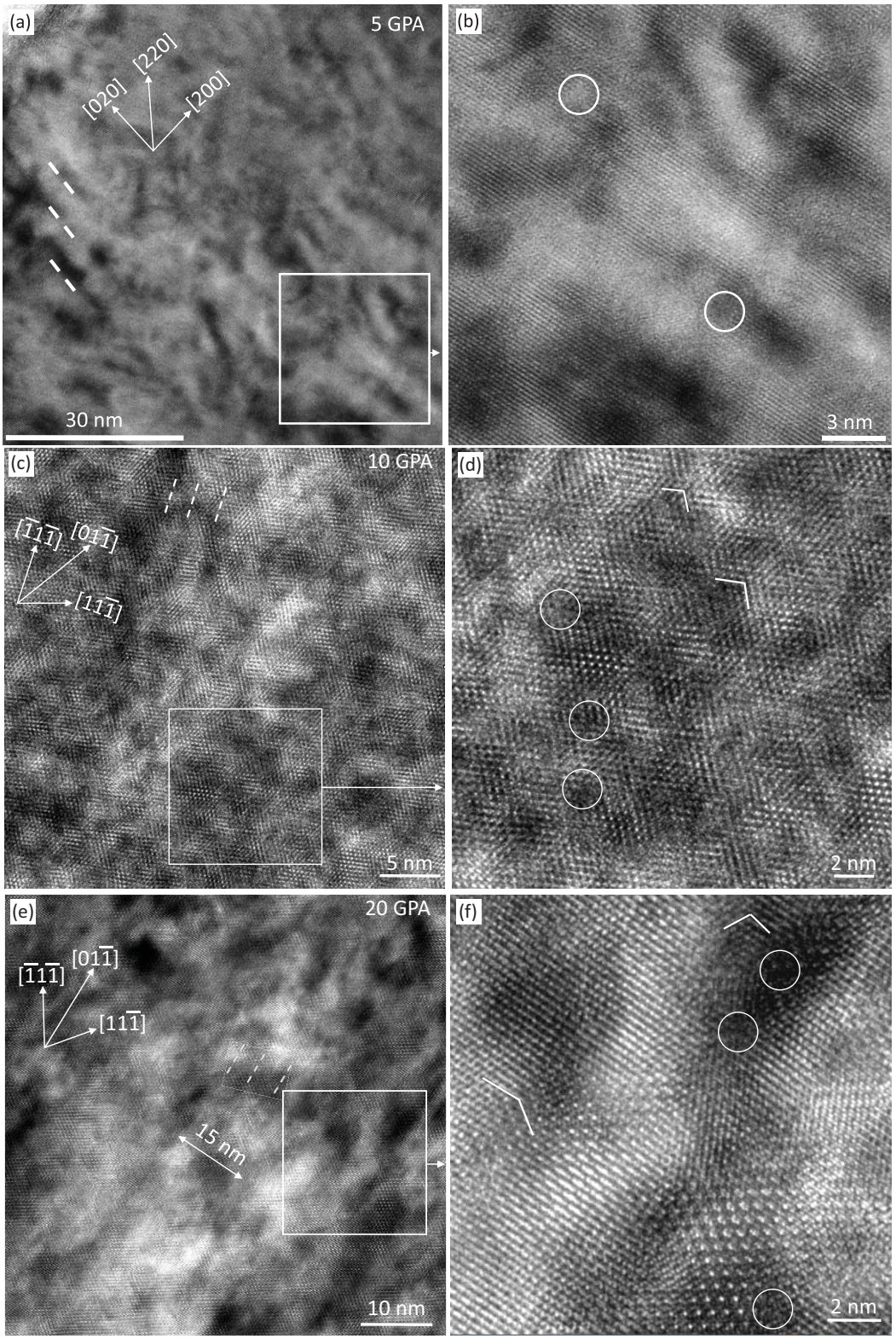

Figure 6. HRTEM micrographs of samples shocked at (a, b) 5, (c, d) 10, and (e, f) 20 GPa. The periodic shear traces are labeled by dashed lines. Circles mark amorphous-like areas containing discontinuous lattice fringes while the curved segments mark zig-zag shaped boundaries between twinned subgrains.

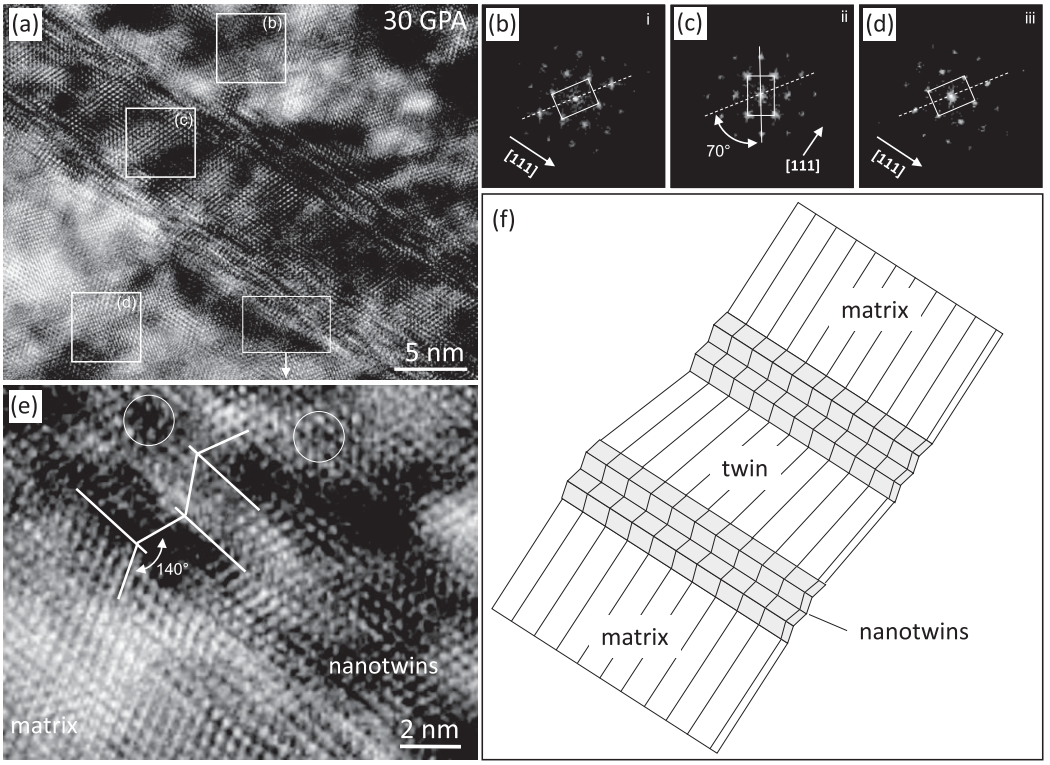

Figure 7. Nanostructure of kink-bands formed at 30 GPa. (a) Multiple twinned subgrains. (b–d) FFT diffractograms from the corresponding boxed areas in Figure 7a, showing that the subgrains are in a twin orientation. (e) An interfacial region between the matrix and a twinned subgrain showing numerous nanotwins (s. white inclined lines) and areas containing discontinuous lattice fringes (circled). (f) Schematic sketch of kink-bands, which formed through plastic buckling. The kink bands are composed of twinned subgrains with nanotwins at their boundaries.

(Figure 8) recover slightly in the same shock pressure regime (above 10 GPa) in which the XRD parameters (Figures 3c and 3d) and the SEM and TEM microscopy data (Figures 4–7) suggest a structural recovery effect.

3.5. FORC Diagrams

First-order reversal curve (FORC) diagrams were analyzed in order to evaluate the shock-induced coercivity changes in more detail (Figure 9). The FORC treatment includes sample mass normalization and the following automatic determination of the smoothing factor SF. The SF value influences the appearance or disappearance of some FORC features, which especially include signals from weak coercivities and the vertical intensity of the strip-shaped scales (Figure 9). However, using this approach, we obtained a clear FORC response on the shock pressure. The initial, preshock magnetite is characterized by a sharply peaked ridge around the $Hc = 0$, spreading parallel to the *Hu* axis. Such behavior is a result of reversible magnetization in self-demagnetizing fields and is typical for MD states [*Pike*, 2003]. Additionally, a weak portion of the FORC signal is occupied parallel to the *Hc* axis. This fact suggests a small portion of relatively hard magnetic carriers like SD or PSD particles probably

Table 2. Hysteresis and Verwey Transition Parameters[a]

Specimen	Mass/ Mass* (mg)	MDS	M_s (Am^2/kg)	M_{rs} (Am^2/kg)	H_c (mT)	H_{cr} (mT)	M_{rs}/M_s (a.u.)	H_{cr}/H_c (a.u.)	χ_{hys} (a.u.)	T_v/T_{fwhm} (K)
Initial	6/234	MD	71.37	1.35	1.22	7	0.019	5.73	1	122/1.5
5 GPa	15/721	PSD	34.52	3.54	8.14	15	0.103	1.84	0.3	128.8/4.3
10 GPa	7/435	PSD	44.21	5.83	16.03	31.6	0.132	1.97	0.26	128/5.9
20 GPa	9/466	PSD	42.35	5.12	17.28	36.83	0.121	2.13	0.25	128.5/4.7
30 GPa	19/446	PSD	12.76	1.53	18.04	39.3	0.119	2.18	0.12	128.3/4.6

[a]Mass corresponds to hysteresis measurements while mass* corresponds to Verwey transition measurements. MDS is the magnetic domain size (MD: multidomain, PSD: pseudosingle domain), *Ms* is the saturation magnetization, M_r is magnetic remanence, H_c is coercivity, H_{cr} is back field coercivity, χ_{hys} is hysteresis susceptibility, *Tv* is Vewey transition temperature, and *Tfwhm is* the transition width measured as a full width at the half maximum (FWHM).

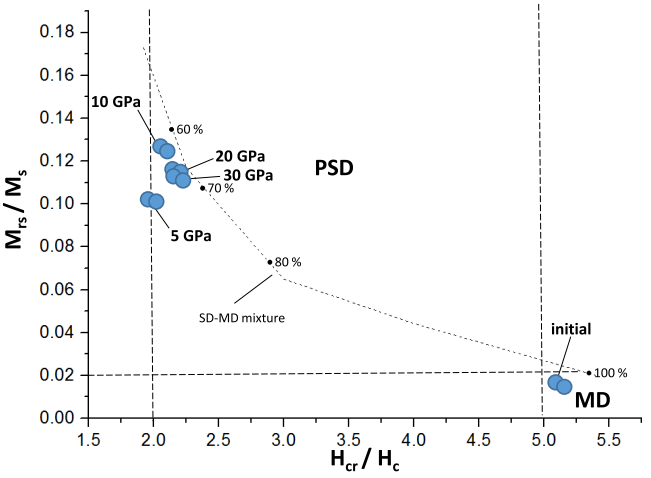

Figure 8. Day plot [after *Day et al.*, 1977] showing shock-induced domain refinement from the MD to the PSD field. The theoretical mixing curve (dashed) is plotted after *Dunlop* [2002].

indicating irreversible movements of magnetic domains pinned at lattice defects [e.g., *Lindquist et al.*, 2015]. As the shock pressure increases, the signal area corresponding to the SD-MD particles becomes larger and more round shaped and moves to higher coercivities *Hc* (Figures 9b–9d). A similar trend was also shown by *Muxworthy and Dunlop* [2002], who studied synthetic magnetite particles in the grain size range between 11 and 0.3 μm. As predicted by the Day plot (Figure 8), we have to consider the presence of mixtures of different magnetic domains sizes. The total area occupied by a FORC signal can be roughly divided into two main partial signals along the *Hc* axis between 0 and 5 T corresponding to MD particles, and above 5 T corresponding to a SD-MD mixture. Based on these considerations, we developed a procedure allowing us to calculate the percentage of the area occupied by a FORC signal by using a binarization algorithm incorporated into the ImageJ software [*Rasband*, 1997]. For this purpose, first, a FORC image was binarized, and

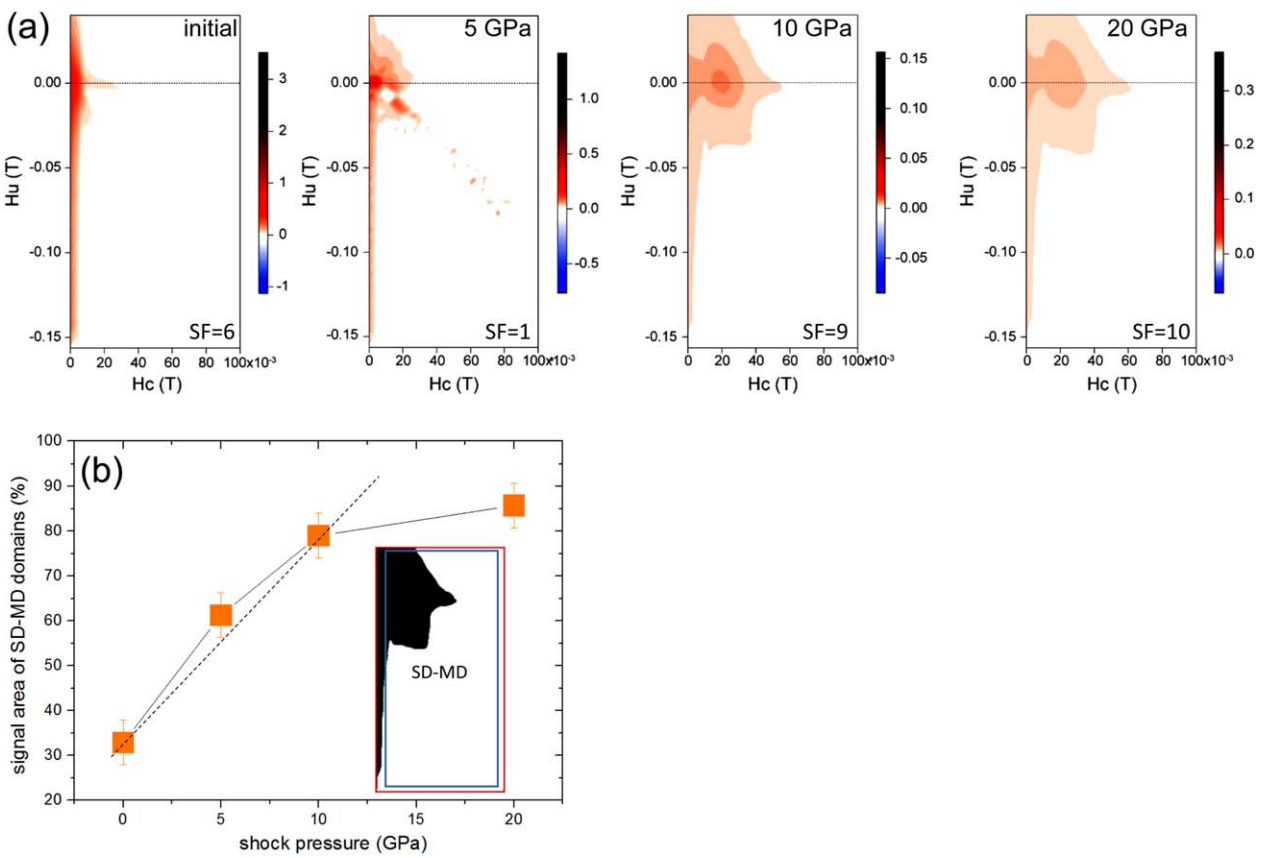

Figure 9. (a) First-order reversal curve (FORC) diagrams as a function of shock pressure. Note that the increasing shock pressure correlate with the increasing signal spreading around the *Hu* = 0, and therefore is mostly proportional to the increasing portion of domains exhibiting PSD or SD-MD-mixture behavior. Automatically determined smoothing factor (SF) values are shown at the bottom of diagrams. (b) Percentage signal area related to SD-MD-domains. The inset is an example of a generated binarized image used a source for the signal area determination using image analysis. The blue frame illustrates the selection of the SD-MD portion for the total signal. The dashed black line marks the linear relationship between the distribution of magnetic domains and shock pressures up to 10 GPa.

then, the percentage of the area of a FORC signal occupied by the SD-MD signal area (see blue frame in Figure 9) was determined as a ratio of black pixels to the total image area (Figure 9b, inset). This approach ignores fine intensity or coercivity variations but is representative for the global FORC changes. Up to 10 GPa, a clear linear correlation between increasing shock pressure and the growing portion of SD-MD signal area (as a measure of the reduction rate) can be recognized (s. the dashed line in Figure 9b). At 20 GPa, the portion of the SD-MD signal is similar to the one at 10 GPa.

3.6. Weak-Field Susceptibility

The effect of shock pressure on the magnetic susceptibility measured around the Verwey transition is shown in Figure 10. The sharp Verwey transition (*Tv*) at 120 ± 2 K for the initial (unshocked) magnetite attests a high chemical purity and crystallization degree of MD magnetite grains in agreement with microprobe analyses and XRD results (see section 2.1). The most prominent shock effect is a drastic drop of magnetic susceptibility around temperatures of 80 and 300 K indicated by dashed arrows in Figure 10. Furthermore, increasing shock pressure correlates with a slight increase of the *Tv* temperature and the broadening of the transition width (Figure 11 and Table 2).

Details of the discovered magnetic modifications are presented in Figure 11. Both, low (80 K) and room (~300 K) temperature magnetic susceptibility rapidly drops in the 5 GPa sample and shows a slightly stronger decrease to its lowest value in the 30 GPa sample (Figures 11a and 11b). The relative changes in susceptibility between low (T_{80K}) and room temperatures (T_{rt}) can be characterized via the *t*-ratio calculated as $(T_{rt} - T_{80K}/T_{rt}) \times 100$. Figure 11c shows that this ratio appears to be more sensitive to shock pressure variations than magnetic susceptibility. For shock pressures up to 10 GPa, the ratio decreases and increases slightly in the 20 and 30 GPa samples.

Less sensitive to the shock pressure is *Tv* (Figure 11d and Table 2). A significant change is only recognized between the unshocked (~122 K) and the shocked samples (~128 K) while within the shocked samples *Tv* remains essentially constant. In contrast, the width of the transition (Figure 11e) appears to be more sensitive to the variation in shock pressure: a parabolic increase from the initial state to 10 GPa is followed by a significant decrease at 20 and 30 GPa. The latter variation suggests again a recovery effect and correlates well with the evolution of the *t*-ratio (Figure 11c).

3.7. Low-Temperature Cycling of SIRM

Low-temperature cycling (LTC) of a room temperature SIRM was used to characterize the ability of shocked magnetite to acquire a magnetic remanence in a strong external magnetic field. For this purpose, the saturated samples were first cooled down from 300 to 20 K and then warmed back to 300 K in zero field. Compared to preshocked magnetite, the shapes of LTC curves of the shocked samples are very different (Figures 12). According to *Bowles et al.* [2012], M1-M6 points can be labeled. During cooling, the original magnetization (M1) of preshocked magnetite reaches a minimum (M2) near *Tv* = 120 K, followed by an increase to a local maximum (M3) and then remains constant to M4 at the minimum temperature at 20 K (Figure 12a).

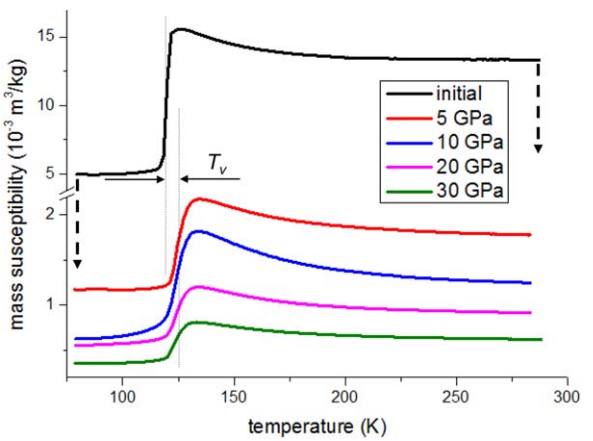

Figure 10. Weak-field susceptibility around Verwey transition as a function of shock pressure. Increasing shock pressure correlates with a drastic drop of susceptibility (dashed arrows), an increasing transition width and a shift in the transition temperature, *Tv*.

On warming, the magnetization is reversible to the cooling curve until M3 and reaches a slightly lower minimum (M5) than during cooling (M2) before reaching the M6 end value at room temperature (Figure 12b). Note that the changes in SIRM on cooling and rewarming below T_V are almost abrupt and perfectly reversible. Such a "jump" on cooling through T_V in a zero field is typical for the cubic-monoclinic transition of large MD magnetite grains or single crystals [*Özdemir and Dunlop*, 1999].

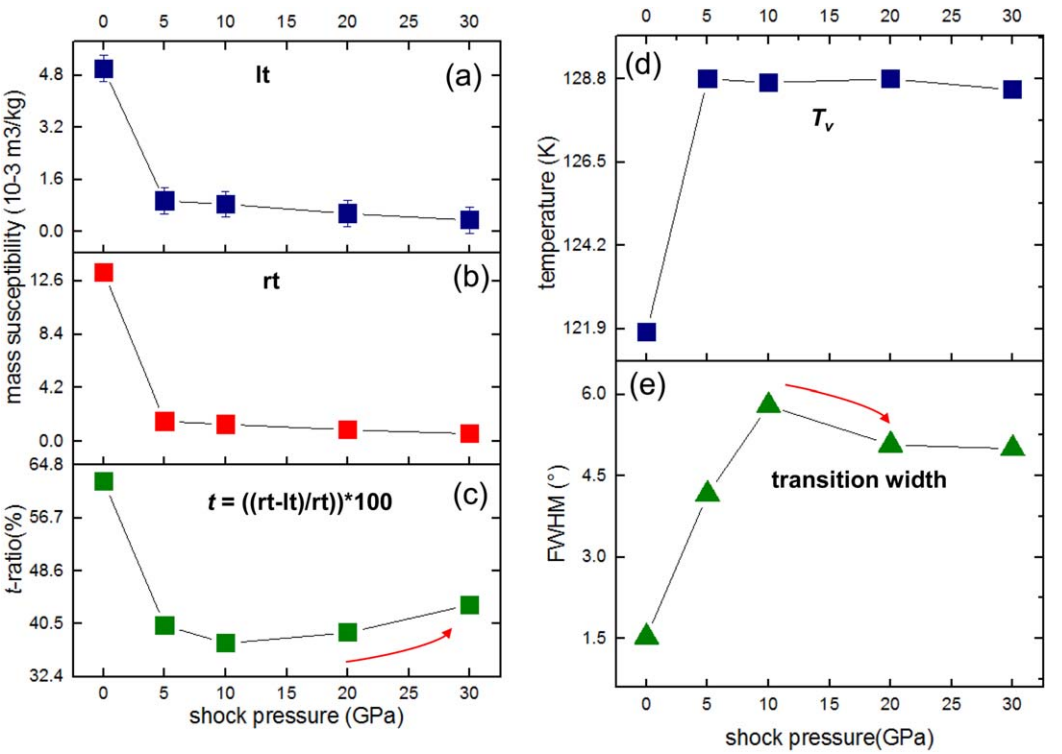

Figure 11. Weak-field susceptibility parameters versus shock pressure. (a) Susceptibility at 80 K (left). (b) Susceptibility at room temperature (right). (c) *t*-ratio. (d) Verwey transition temperature, *Tv*. (e) Transition width measured as a FWHM of first derivative curves. Red arrows indicate possible recovery effects.

In contrast to the preshocked sample, the cooling-warming curves of shocked magnetite are extremely irreversible around the isotropic point T ~ 130 K and they exhibit a strong increase of the M1, M4, and M6 values as a function of pressure (see the dashed arrows in Figure 12) suggesting an increase of magnetic memory [*Özdemir and Dunlop*, 1999; *Muxworthy et al*., 2003; *Bowles et al*., 2012]. A closer look reveals some additional important information of the transition character in relation to the shock pressure. In the cooling curves (Figure 12a), the M3 point is relatively weak developed in the shocked samples. This behavior is typical for SD-PSD particles [*Özdemir and Dunlop*, 1999; *Muxworthy et al*., 2003; *Bowles et al*., 2012]. In this case, rotation of the individual particle moments into *c* axis alignment causes a loss of room temperature SIRM, as some of the magnetization is effectively randomized. As a result, there is no well-defined transition from monoclinic to cubic phase, i.e., the Verwey transition is degenerated. In contrast, in the warming curves (Figure 12b), the M3 point appears to be increasingly pronounced with increasing shock pressures. Furthermore, two Verwey transition temperatures, T_{V1} (120 K) and T_{V2} (112 K, low temperature), can be recognized in the cooling curves of the samples shocked to 5 and 10 GPa (Figure 12a). After subsequent warming, the second T_{V2} transition is no more detectable (Figure 12b). The 20 and 30 GPa samples are characterized by a single, regular Verwey transition (Figure 12a).

The quantitative relationship between magnetic memory and shock pressure is shown in Figure 13. First, the magnetic capacity is characterized by the SIRM magnetic memory ratio *m* (Figure 13b). In a similar way as it is used elsewhere [e.g., *Muxworthy et al*., 2003], this ratio is defined as (M6/M1) × 100 and reflects the amount of the recovered magnetic memory acquired after a cooling-warming cycling. With increasing shock pressure the *m*-ratio increases (black symbols in Figure 13). This relationship clearly demonstrates the increasing capacity of shocked magnetite to acquire a laboratory imparted magnetic remanence. Note, that the *m*-ratio increases nearly linear up to 20 GPa (to about 53% of its initial SIRM), and drops slightly at 30 GPa (Figure 13, black symbols).

As it was mentioned above, there is a slight development of the jump around the M3 and M5 points in the warming curves (Figure 12b). In order to evaluate this jump, we introduce a *j*-ratio, which corresponds to the jump height or to the difference between the M5 and M1 values. As it can be seen from Figure 13 (blue

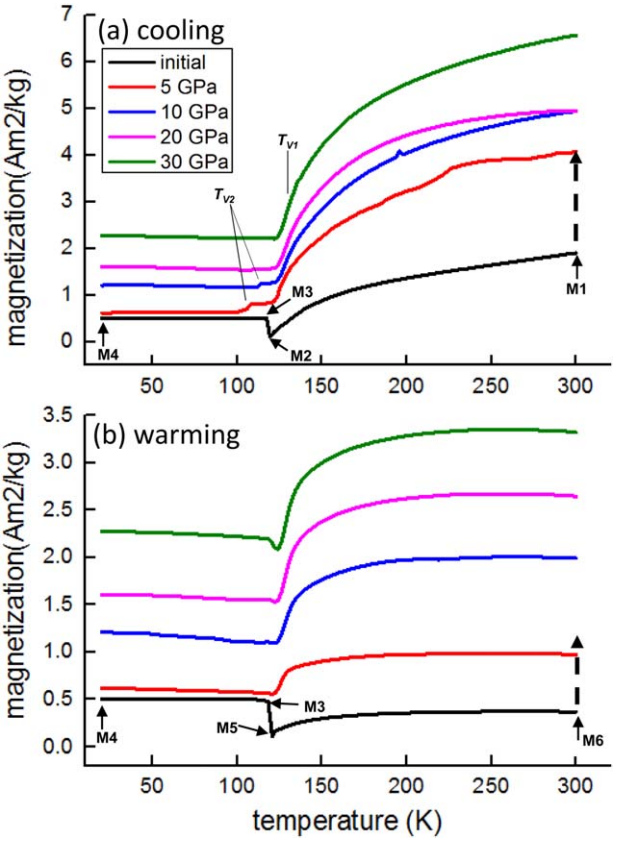

Figure 12. Effect of shock pressure on the low-temperature cycling of SIRM created in a magnetic field of 2.5 T at 300 K. Note the prominent magnetization increase (see dashed lines) in the shocked samples. T_{V1}—high-temperature, regular Verwey transition, T_{V2}—second, low-temperature Verwey transition. M1-M6 are characteristic features labeled according to *Bowles et al.* [2012] and described in the text.

symbols), the *j*-ratio (normalized to the initial value of the preshocked sample) abruptly decreases from the initial to the 5 GPa sample. Starting at 10 GPa the *j*-ratio increases again to about 25% (30 GPa sample) of the initial value of the preshocked sample.

4. Discussion

We studied for the first time systematic modifications of mineralogical, microstructural, and magnetic properties in magnetite, experimentally shocked to pressures of 5, 10, 20, and 30 GPa. No high-pressure phase of magnetite or another Fe oxide (e.g., maghemite and hematite) than cubic stoichiometric magnetite, albeit with a slightly distorted lattice, was identified by XRD, electron microprobe analysis and Mössbauer analysis (not shown here) and therefore no mineralogical change occurred in shocked magnetite up to 30 GPa. Magnetic properties indicate a PSD grain size for all shocked samples and suggest that strongest changes occur in the 5 or 10 GPa sample, while the 20 and 30 GPa sample always show a recovery in magnetic properties compared to the initially polycrystalline, multidomain magnetite. This observation suggests that in the high-shock pressure regime deformation mechanisms change, which influences the magnetic properties in the direction of slightly larger magnetic domain sizes. While grain fragmentation and accumulation of lattice defects along microshear bands occur in all shocked samples, mechanical twin lamellae formation parallel to the [−11 −1] direction starts to develop at 10 GPa. This twinning law is also characteristic for mechanical twinning in spinel above 25.5 GPa, where it is suggested as characteristic phenomenon for shock deformation [e.g., *Schäffer et al.*, 1983]. Mechanical twinning in magnetite is however already reported from deformation experiments (0.5 GPa, 20°C) by *Henning-Michaeli and Siemes* [1975] and therefore occurs already at lower stresses, probably because the Mohs hardness is much lower for magnetite (5.5) than for spinel (8.5). All samples from our study have exceeded the Hugoniot elastic limit and suffered brittle and plastic deformation to different degrees. Melt globules along

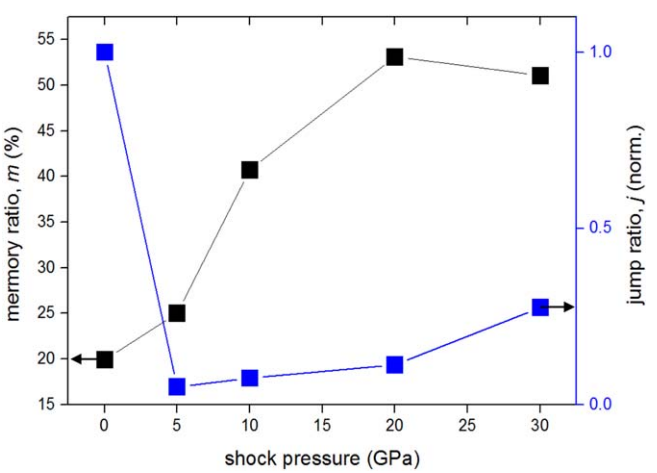

Figure 13. Effect of shock pressure on the demagnetization parameters including SIRM memory ratio *m* (black symbols) and the jump ratio, *j* (blue symbols).

Table 3. Compilation of Shock Effects in Magnetite[a]

	Shock Stages			
	5 GPa	10 GPa	20 GPa	30 GPa
Magnetic behavior	Verwey Transitions T_{V1} increases T_{V2} in SIRM curves Hysteresis Parameters H_c and H_{cr} *increase* while χ and M_s *decrease* M_{rs} *increases* Magnetic Memory (SIRM Measurements) *m-ratio increases* Magnetic Domain State (FORC Measurements) SD/MD ratio increases	Transition width at T_{V1} *largest* T_{V2} in SIRM curves	Transition width at T_{V1} *recovers* T_{V2} *disappears* in SIRM curves *m-ratio saturates* SD/MD ratio saturates	Transition width at T_{V1} *recovers* T_{V2} *disappears* in SIRM curves M_{rs} *recovers*
Brittle deformation	Grain fracturing Drop of apparent crystallite size and lattice constant	Grain fracturing Apparent crystallite size *lowest*	Intensive grain fragmentation	
Plastic deformation	Shear bands	Shear bands, microtwins	Growth of shear bands, kink-bands composed of multiple twinned subgrains	
Amorphization	Mosaics containing clusters with point defects		Molten globules	

[a]Initial material was polycrystalline multidomain. T_{v1} *and* T_{v2} are two Verwey transitions in SIRM curves (see Figure 12); SD—single domains; MD—multidomains, while their SD/MD ratio is extracted from FORC data (see Figure 9); M_s is the saturation magnetization, M_{rs} is magnetic remanence, H_c is coercivity, H_{cr} is back field coercivity, and χ_{hys} is hysteresis susceptibility (see Table 2); *m*—magnetic memory ratio extracted from SIRM data (see Figure 13).

shear band terraces indicate beginning amorphization at 20 GPa. Table 3 summarizes the deformation phenomena and related magnetic property modifications in the shocked magnetite.

4.1. Magnetic Domain Structure Refinement of Shocked Magnetite

The most prominent modification in magnetic parameters is related to a multidomain (MD) to pseudosingle-domain (PSD) or single-domain (SD) grain size reduction, visible in the decrease of magnetic susceptibility and an increase of coercivity, signal area of SD-MD domains from FORC diagrams and magnetic memory from SIRM cooling-warming cycles (Table 2 and Figures (9 and 11), and 13) with a maximum in the 10 or 20 GPa sample. This observation is in agreement with the occurrence of the smallest X-ray apparent crystallite size of 80 nm in the 10 and 20 GPa sample (Figure 3c). This size is above the critical single domain grain size for magnetite of 50–60 μm [*Dunlop and Özdemir*, 1997], and explains why in FORC diagrams (Figure 9a) no superparamagnetic fraction is observable. The 10 and 20 GPa FORC diagrams with their closed contour peaks at about 20 mT resemble to those shown in *Muxworthy and Dunlop* [2002] for pseudosingle domain grains of the size 1.7–7 μm. *Dunlop and Özdemir* [1997] showed that this grain diameter corresponds to coercive forces between around 8 and 18 mT for natural crushed magnetite crystals, which is in good agreement to the coercive forces in our study (see Table 2). Interestingly, the FORC diagrams clearly show a MD fraction additional to the newly formed SD or PSD fractions in all shocked samples up to 30 GPa suggesting a strongly heterogeneous distribution of magnetic domain and grain sizes. According to the calculations [e.g., *Fritz et al.* 2011], the shock pressure inside the target however, was relatively homogeneous distributed. Therefore, the large grain and magnetic domain size variation seen in our experiments is suggested to be a typical shock-related phenomenon at each shock pressure stage. In our shocked magnetite, not only grain crushing but also plastic deformation microstructures such as mosaic subgrains or twins (Figures 6 and 7) contribute to the increase of coercivity. This conclusion is in agreement with observations of *Lindquist et al*. [2015] who reported a slight coercivity increase in MD magnetite due to dislocation interactions with domain walls. The quantification of FORC area distribution (Figure 9b) seems to show a good sensitivity to the shock-induced refinement of magnetic domains, albeit the complexity of shock-induced grain refinement by brittle and plastic deformation mechanisms is not completely revealed.

4.2. Shock-Induced Microstructural Changes

Magnetic domain structures in magnetite are very sensitive to lattice defects and internal stress [*Dunlop and Özdemir*, 1997]. SEM and TEM observations of our study have shown that plastic deformation phenomena like shear bands starting at 5 GPa and twins starting at 10 GPa occur in the micrometer to nanometer-scale range. Similar to our study, *Schäffer et al*. [1983] describe for shocked spinel deformation twin lamellae and a strongly heterogeneous defect density distribution albeit at much higher-shock pressures. This inhomogeneity and the early occurrence of twins as soon as the elastic limit has been exceeded are expected to

hinder the use of shock-induced twinning in spinel as a shock barometer [*Schäffer et al*., 1983]. The onset of twinning is not only shock pressure dependent but the twinning threshold also depends on grain size [e.g., *Murr and Esquivel*, 2004, and references therein]. According to *Armstrong and Worthington* [1973], the necessity of microslip for twin initiation is another important effect for twinning. Although the two latter studies refer to metal and alloys we see in our study on shocked magnetite essentially the same evolution of shock deformation features. To our knowledge, we show for the first time shock-induced plastic deformation like microshear bands and mechanical twinning in magnetite for well-defined shock pressures. Unfortunately, these plastic deformation features cannot be observed under the optical microscope. But our study shows that microshear bands and even twins can be easily detected on fresh, shock-fracture related surfaces using SEM (Figure 4), which provides a fast and nondestructive method for identification of shock-induced deformation phenomena. Under TEM, the onset of twin formation in shocked magnetite can be recognized as zig-zag shaped structures (see the curved segments in Figure 6b). At 20 GPa, the size of the zig-zag shaped structures increases (Figure 6b) and at 30 GPa, well-developed multiply twinned lamellae and kink-bands are formed (Figures 4d and 7). Furthermore, the direct local SEM and TEM observations of twins correlate well with the Williamson-Hall plots suggesting a bulk heterogeneous strain accumulation in the shocked samples (Figure 3c). Microshear bands and twinning are suggested to be precursors of dynamic recrystallization in impact crater materials and a general phenomenon of shocked material [e.g., *Murr and Esquivel*, 2004]. *Cloete et al*. [1999] indeed observed twins in magnetite using TEM from the Vredefort impact structure. Magnetite occurs there as inclusions in quartz and the twins are interpreted to be shock induced.

4.3. Strain Memory Effect

During shock reverberation experiments, decompressed samples are produced, which are similar to impact rocks. *Carporzen and Gilder* [2010] suggested a shift in the Verwey transition (T_V) with increasing static pressure as an indicator for a strain memory in magnetite and found for decompressed stoichiometric magnetite in the pressure range up to 5 GPa an increase of T_V of 1 K/GPa. *Coe et al*. [2012] confirmed the increase of T_V in stressed magnetite but reported a relatively large variation of T_V slope from -6 to $+16$ K/GPa. This large variability is explained by the favoring of some monoclinic twins over others as they form under deviatoric stresses at T_V.

T_V from all shocked magnetite of our study is increased by about 6 K compared to the initial magnetite (Figure 11d and Tables 2 and 3) and no significant change with different shock pressure is indicated. If this phenomenon is a strain effect as suggested by *Carporzen and Gilder* [2010] and *Coe et al*. [2012], this observation suggests that nonpermanent deformation is similar in all shocked magnetite samples and reaches already at 5 GPa some kind of saturation. In addition to the increase in T_V a broadening of the transition is observed, which is also attributed to internal stresses caused by shock-induced crystal defects [*Carporzen and Gilder*, 2010; *Coe et al*., 2012]. *Carporzen and Gilder* [2010] pointed out that the width of the transition seems to reflect the cumulative strain state of magnetite, where domain wall pinning plays an important role, and therefore it is more sensitive than the transition temperature itself. This statement correlates well with our results shown in Table 2 and Figure 11d. Additionally, Figure 11d shows that the strongest broadening is observed in the 10 GPa sample while in the 20 and 30 GPa sample the broadening is reduced again. This observation agrees well with the trends of apparent crystallite size and lattice constant for the shocked magnetite (Figures 3c and 3d) and suggests that lattice distortion (elastic strain) and grain refinement by brittle and plastic deformation mechanisms is largest in the 10 GPa magnetite, while at 20 and 30 GPa plastic deformation mechanism like twin domain growth increase crystallite size again (Table 3). Therefore, different deformation mechanism superimposes each other, which all effect the T_V of magnetite. One interesting observation is that in SIRM cooling a second T_{V2} is observed at lower temperature (112 K) in the 5 and 10 GPa magnetite, which vanishes in the warming curve. A decrease of T_V is reported in static pressure experiments by *Todo et al*. [2001] and *Rozenberg et al*. [2006] in the pressure range up to 8 and 12 GPa, respectively, and is related to a disordered state of Fe^{2+} and Fe^{3+} valence on B sites in the stressed magnetite lattice. This second T_{V2} is not observed in the low-temperature magnetic susceptibility curve (Figure 10), which also is a warming up curve. We suspect this second T_{V2} to be related to the stressed magnetite crystals and believe that during a first T_{V1} cooling this stress is released due to the cubic to monoclinic phase transition including a reordering of the different iron valence.

If this interpretation is true, elastic strain in magnetite changes during crossing T_V and might not be used as strain memory in dependence of pressure as suggested by *Carporzen and Gilder* [2010]. In contrast to the

observations by *Carporzen and Gilder* [2010] heat treatment up to 700°C of our shocked magnetite samples cause a lowering of the T_V temperature nearly to the original value of the initial unshocked magnetite (not shown here). We interpret this behavior as annealing effect on magnetite, which removes the strain memory. This aspect of our study will be discussed in more detail in a follow up article.

An interesting observation from our study is the strong decrease of saturation magnetization (M_S) in shocked compared to initial magnetite (Table 2). Although M_S is reported to be a material constant for magnetite [e.g., *Dunlop and Özdemir*, 1997; *Williams and Dunlop*, 1995] there are some studied reporting a decrease of this parameter. For example, *Nagata and Kinoshita* [1964] already demonstrate a clear M_S decrease with pressure, which they relate to mechanical stress. *Thapa et al*. [2004] show in a study on different sizes of synthetic magnetite nanoparticles first an increase of M_S, and below a size of 10 nm a significant reduction of more than 50%. These significant changes are attributed to surface effects, which decrease magnetization, probably due to a higher concentration of Fe^{3+} valances at the surface of the small grains. As the 5, 10, and 20 GPa samples show a similar decrease in M_S, the 30 GPa sample displays a significant stronger decrease (Table 2). We suspect that the first decrease in the 5, 10, and 20 GPa magnetite samples is dominantly influenced by elastic strain, while in the 30 GPa sample amorphization strongly superpose this effect. Both, elastic strain and amorphization reduce M_S. Although we do not see a superparamagnetic contribution in the FORC diagrams (Figure 9), an increasing portion of nanosized particles is documented by our TEM results (e.g., Figure 7). High concentrations of surface defects along the shear bands and twin boundaries might be in addition responsible for the *Ms* drop.

4.4. Phase Transition, Decompression, and Amorphization

Magnetite exhibits a high-pressure, cubic to monoclinic phase transition at 25 GPa under room temperature conditions [*Olsen et al*., 1994], above which the Fe_3O_4 sluggishly transforms into an insulating perovskite-like phase [*Rozenberg et al*., 2006]. From extrapolations >25 GPa, a total loss of ferromagnetic moments is suggested to occur around 70 GPa [*Baudelet et al*., 2010], indicating that the magnetic structure of magnetite is very stable under static pressure. However, T_V is described to be pressure dependent as described already above. In contradiction to *Coe et al*. [2012] and *Carporzen and Gilder* [2010], *Todo et al*. [2001] describes a decrease of T_V with increasing pressure until it disappears above 8 GPa. This behavior suggests that at static pressures >8 GPa no insulator—metal transition occurs any more at low temperatures in magnetite. Decompressed samples however do not show this behavior as it is shown in our study and in the study of *Carporzen and Gilder* [2010] and it remains an open question if magnetite undergoes a reversible magnetic phase transition at pressures above 5–8 GPa in shock reverberation experiments.

A comparison of diffraction peaks between quartz, which is intergrown with magnetite in our shocked samples (see Figure 1), and magnetite (Figure 3b) show profound shift and broadening of peaks in both minerals. The maximal broadening of the (21-1) quartz peak at 30 GPa correlates well with the abundant occurrence of planar deformation features (PDFs) under the optical microscope (not shown here). According to *Langenhorst* [1994], the appearance of PDFs is characteristic for shock pressures around 20 GPa. Therefore, the formation of PDFs accompanied by broadening of X-ray peaks of quartz is in agreement with the calculated pressure values given in Table 1 and we are confident that our 30 GPa sample reached the pressure threshold at which the high-pressure phase transition should occur. However, no high-pressure phase with another than cubic (but distorted) symmetry has been observed in our study. The broadening of diffraction peaks in magnetite is interpreted in our study to be the result of partial amorphization additional to grain reduction and strain in magnetite.

A strong argument for a localized shock melting is the occurrence of globular magnetite grains along sheared terraces in the 20 GPa sample observed by SEM (Figure 4c). Under the TEM, amorphous clusters indicating lattice disordering were also observed along the <110> directions in shear bands as well as randomly distributed (Figure 6). This is especially conspicuous for the 20 GPa magnetite sample (Figures 6c and 6d). Our TEM observations for magnetite are similar to those of *Ashworth and Schneider* [1985] for experimentally shocked quartz. Their TEM investigations revealed glass lamellae, which can be correlated with optical planar elements and surface steps seen in SEM and they interpreted the sharply defined lamellae to result from vitrification as direct consequence of deformation. The increasing defect density in the deformation lamellae is a precursor of pervasively disordering and amorphization. Amorphous clusters at the nanometer scale were also reported by *Mang et al*. [2013] in shocked pyrrhotite as planar deformation

features at 8 GPa or as randomly distributed amorphous areas at 20 GPa. Furthermore, *Mang et al*. [2013] report that at pressures of 20 GPa upward mechanical twinning is a dominant shock-induced feature in pyrrhotite besides amorphization. These observations are similar to those of the present study for magnetite (Figures 4d, 6, and 7) and suggest that the dynamic deformation phenomena are similar in different magnetic minerals.

Our measurements of the postshock container temperature (see section 2.2) suggest the presence of a low temperature, 95°C annealing after shock. However, we have strong microstructural arguments for much higher temperatures such as globular grains at sheared terraces (Figure 4c) and amorphous, nanosized clusters containing point defects (Figures (6 and 7)). *Langenhorst* [1994] presented calculations of shock temperatures for quartz (melting point ~ 1720°C) subjected to laboratory shock waves. These results show the shock pressure increase from 10 to 30 GPa is the reason of the shock temperature increase from ~250 to 1600°C, respectively [*Langenhorst*, 1994]. *Ugalde et al*. [2005] carried out numerical calculations of pressure-temperature profiles occurring during meteorite-like projectile on a diabase target and obtained very similar results. The physical and mechanical properties of the studied quartz-magnetite banded ore can be roughly compared with those for quartz or diabase. Therefore, one can assume that depending on the applied shock pressure, the shock temperatures in our experiments were approximately between 250 and 1500°C. Molten magnetite grains at shear terraces (Figure 4d) suggest localized melting of magnetite, which has a melting point of about 1538°C [*Mineral Data*]. Local temperature spikes might be favored at frictional surfaces like the shear bands (Figures 5–7). They are also suggested in the studies of, e.g., *Mang et al*. [2013] on experimentally shocked pyrrhotite and *Agarwal et al*. [2016] on naturally shocked dolerite from the Lockne impact structure, Sweden. Based on our results we conclude that the shock-induced temperature as well as shear movements, probably along subgrain boundaries in magnetite, favor amorphization or local melting which are not typical for static, elastic loading experiments reported elsewhere [*Gilder et al*., 2002, 2004; *Carporzen and Gilder*, 2010].

5. Conclusions

Investigations of mineralogical, microstructural and magnetic properties in polycrystalline, multidomain magnetite experimentally shocked to pressures of 5, 10, 20, and 30 GPa revealed that no high-pressure phase of magnetite occurs and that all samples show inhomogeneous distributed permanent brittle and plastic as well as nonpermanent deformation features along with a beginning amorphization at 20 GPa in a slightly distorted stoichiometric magnetite lattice. The spatial inhomogeneity of shock effects is indicated by the asymmetric broadening of X-ray peaks and is similar to observations of *Ashworth and Schneider* [1985] for quartz. These microstructural phenomena strongly control the magnetic properties of magnetite, which are sensitive to a grain refinement due to brittle and plastic deformation (microshear band and twins). This grain refinement is accompanied by a MD to PSD/SD grain size reduction, which is seen in hysteresis parameters as well as in SIRM low-temperature cycling with a significant increase in magnetic memory. While the phenomenon of more single domain like behavior after pressure cycling is known, we provide direct evidence on the mechanism behind the apparent grain size reduction.

Two different T_V were observed in the 5 and 10 GPa sample: a lower one (112 K), which is only seen during cooling and vanishes crossing the transition on warming, and a second T_{V2} at slightly higher temperatures (128 K) than the regular one. We only can speculate that the lower T_{V2} is related to strain in the cubic magnetite lattice which relax during transformation into the monoclinic phase, while the higher T_V might be an effect of the lattice distortion (Figure 3d). A similar shift of about 6 K in T_V for all shock pressure stages compared to the initial magnetite is a qualitative indicator for a strain memory in magnetite in agreement with earlier studies of *Carporzen and Gilder* [2010]. However, we have not found a systematic increase in T_V in the shock pressure range between 5 and 30 GPa and therefore postulate that T_V in this dynamic shock pressure range cannot be used as geobarometer because strain memory saturation occurs already up to 5 GPa. Additionally, from the LT measurements across the Verwey transition, we established that the *t*-ratio and *j*-ratio as well as the transition width provide a sensitive quantitative technique for detecting variations in shock pressure.

A most surprising result of our study is the significant decrease of *Ms* with increasing shock pressure (Table 2). We suggest that especially the 30 GPa sample does no longer correspond to well-crystallized defect-free magnetite but to a distorted and damaged magnetite lattice, containing significant amounts of internal defects and amorphous regions (Figures 3–7), which modifies magnetic properties of shocked magnetite.

In this study, these effects are reported for the first time for a shock-loaded magnetite, and obviously are nonspecific for static loaded magnetite. It should be noted that X-ray diffraction (Figure 3) and the applied magnetic methods (Figures 8–13) provide bulk information of the overall shock-induced effects. These bulk data are in a good accordance with our HRTEM results (Figures 5–7) providing direct information on the type of lattice defects. Because the brittle and plastic deformation phenomena are heterogeneously distributed within the magnetite grains in the different shock stages, a serious use of magnetic properties as geobarometer without knowledge of the corresponding microstructural phenomena is strongly hampered. This study clarifies the different deformation mechanisms operating with shock pressure in magnetite and provide a solid base for interpretations of magnetic properties from impact structures with magnetite-bearing rocks on earth and in shocked meteorites.

Acknowledgments
This work was funded by the priority program Planetary Magnetism of the DFG (project KO1514/8: "Mineral magnetism of shocked ferrimagnetic minerals"). We are grateful to B. Priesemann from the Helgeland Museum, Norway, for kindly providing the magnetite ore samples, and to A. Holzwarth from the Ernst-Mach Institute, Freiburg, for conducting the shock experiments. We thank the members of the Institute for Rock Magnetism for a fellowship that was given to A.K. in October 2014 and especially Mike Jackson for his large support during the time of the stay. Thanks to Jerome Gattacceca and an anonymous reviewer for their constructive comments, which significantly improved the manuscript. We confirm that all the numerical information provided in the figures is produced by solving the equations given in the paper.

References

Agarwal, A., B. Reznik, A. Kontny, S. Heissler, and F. Schilling (2016), Lingunite a high-pressure plagioclase polymorph at mineral interfaces in doleritic rock of the Lockne impact structure (Sweden), *Sci. Rep.*, *6*, 25991, doi:10.1038/srep25991.

Alexander, L., and H. P. Klug (1950), Determination of crystallite size with the x-ray spectrometer, *J. Appl. Phys.*, *21*(2), 137–142, doi:10.1063/1.1699612.

Armstrong, R. W., and P. J. Worthington (1973), *Metallurgical Effects at High Strain Rates*, edited by R. W. Rohde, et al., pp. 401–414, Springer, Boston, Mass.

Ashworth, J. R., and H. Schneider (1985), Deformation and transformation in experimentally shock-loaded quartz, *Phys. Chem. Miner.*, *11*(6), 241–249, doi:10.1007/BF00307401.

Baudelet, F., S. Pascarelli, O. Mathon, J.-P. Itié, A. Polian, and J.-C. Chervin (2010), Absence of abrupt pressure-induced magnetic transitions in magnetite, *Phys. Rev. B*, *82*(14), 140412, doi:10.1103/PhysRevB.82.140412.

Bezaeva, N. S., P. Rochette, J. Gattacceca, R. A. Sadykov, and V. I. Trukhin (2007), Pressure demagnetization of the Martian crust: Ground truth from SNC meteorites, *Geophys. Res. Lett.*, *34*, L23202, doi:10.1029/2007GL031501.

Bowles, J., M. Jackson, and L. Brown (2012), The magnetite Verwey transition, *IRM Q.*, *22*(2), 1–12.

Carporzen, L., and S. A. Gilder (2010), Strain memory of the Verwey transition, *J. Geophys. Res.*, *115*, B05103, doi:10.1029/2009JB006813.

Cloete, M., R. J. Hart, H. K. Schmid, M. Drury, C. M. Demanet, and K. V Sankar (1999), Characterization of magnetite particles in shocked quartz by means of electron- and magnetic force microscopy: Vredefort, South Africa, *Contrib. Mineral. Petrol.*, *137*(3), 232–245, doi:10.1007/s004100050548.

Coe, R. S., R. Egli, S. A. Gilder, and J. P. Wright (2012), The thermodynamic effect of nonhydrostatic stress on the Verwey transition, *Earth Planet. Sci. Lett.*, *319-320*, 207–217, doi:10.1016/j.epsl.2011.11.021.

Day, R., M. Fuller, and V. A. Schmidt (1977), Hysteresis properties of titanomagnetites: Grain-size and compositional dependence, *Phys. Earth Planet. Inter.*, *13*, 260–267.

Dunlop, D., and Ö. Özdemir (1997), *Rock Magnetism: Fundamentals and Frontiers*, Cambridge Univ. Press, Cambrige, U. K.

Dunlop, D. J. (2002), Theory and application of the Day plot (Mrs/Ms versus Hcr/Hc) 2. Application to data for rocks, sediments, and soils, *J. Geophys. Res.*, *107*(B3), 2057, doi:10.1029/2001JB000487.

Fritz, J., K. Wünnemann, W. U. Reimold, C. Meyer, and U. Hornemann (2011), Shock experiments on quartz targets pre-cooled to 77 K, *Int. J. Impact Eng.*, *38*(6), 440–445, doi:10.1016/j.ijimpeng.2010.10.014.

Gattacceca, J., A. Lamali, P. Rochette, M. Boustie, and L. Berthe (2007), The effects of explosive-driven shocks on the natural remanent magnetization and the magnetic properties of rocks, *Phys. Earth Planet. Inter.*, *162*(1-2), 85–98, doi:10.1016/j.pepi.2007.03.006.

Gilder, S. A., M. LeGoff, J. Peyronneau, and J.-C. Chervin (2002), Novel high pressure magnetic measurements with application to magnetite, *Geophys. Res. Lett.*, *29*(10), doi:10.1029/2001GL014227.

Gilder, S. A., M. LeGoff, J.-C. Chervin, and J. Peyronneau (2004), Magnetic properties of single and multi-domain magnetite under pressures from 0 to 6 GPa, *Geophys. Res. Lett.*, *31*, L10612, doi:10.1029/2004GL019844.

Hennig-Michaeli, Ch., and H. Siemes (1975), Zwillungsgleitung beim Magnetit, *N.Jb. Miner. Abh. 123*, 330–334.

Hargraves, R. B., and W. E. Perkins (1969), Investigations of the effect of shock on natural remanent magnetism, *J. Geophys. Res.*, *74*(10), 2576–2589, doi:10.1029/JB074i010p02576.

Harrison, R. J., and J. M. Feinberg (2008), FORCinel: An improved algorithm for calculating first-order reversal curve distributions using locally weighted regression smoothing, *Geochem. Geophys. Geosyst.*, *9*, Q05016, doi:10.1029/2008GC001987.

Kohout, T., L. J. Pesonen, A. Deutsch, K. Wünnemann, D. Nowka, U. Hornemann, and E. Heikinheimo (2012), Shock experiments in range of 10-45GPa with small multidomain magnetite in porous targets, *Meteorit. Planet. Sci.*, *47*(10), 1671–1680, doi:10.1111/maps.12003.

Langenhorst, F. (1994), Shock experiments on pre-heated α- and β-quartz: II. X-ray and TEM investigations, *Earth Planet. Sci. Lett.*, *128*(3-4), 683–698, doi:10.1016/0012-821X(94)90179-1.

Lindquist, A. K., J. M. Feinberg, R. J. Harrison, J. C. Loudon, and A. J. Newell (2015), Domain wall pinning and dislocations: Investigating magnetite deformed under conditions analogous, *J. Geophys. Res. Solid Earth*, *120*, 1415–1430, doi:10.1002/2014JB011335.

Louzada, K. L., S. T. Stewart, B. P. Weiss, J. Gattacceca, and N. S. Bezaeva (2010), Shock and static pressure demagnetization of pyrrhotite and implications for the Martian crust, *Earth Planet. Sci. Lett.*, *290*(1-2), 90–101, doi:10.1016/j.epsl.2009.12.006.

Louzada, K. L., S. T. Stewart, B. P. Weiss, J. Gattacceca, R. J. Lillis, and J. S. Halekas (2011), Impact demagnetization of the Martian crust: Current knowledge and future directions, *Earth Planet. Sci. Lett.*, *305*(3-4), 257–269, doi:10.1016/j.epsl.2011.03.013.

Mang, C., and A. Kontny (2013), Origin of two Verwey transitions in different generations of magnetite from the Chesapeake Bay impact structure, USA, *J. Geophys. Res. Solid Earth*, *118*, 5195–5207, doi:10.1002/jgrb.50291.

Mang, C., A. Kontny, J. Fritz, and R. Schneider (2013), Shock experiments up to 30 GPa and their consequences on microstructures and magnetic properties in pyrrhotite, *Geochem. Geophys. Geosyst.*, *14*, 64–85, doi:10.1029/2012GC004242.

Marsh, S. P. (1980), *LASL Shock Hugoniot Data*, Univ. Calif. Press, Berkeley.

Mineral Data, Melting points of some compounds and minerals. [Available at http://www.ceramicindustry.com/ext/resources/CI/Protected/Files/PDF/meltingpoints_compounds-materials.pdf.]

Muller, W. F., and U. Hornemann (1969), Schock-induced planar deformation structures in experimentally shock-loaded olivines and in olivines from chondritic meteorites, *Earth Planet. Sci. Lett.*, *7*, 251–264.

Murr, L. E., and E. V. Esquivel (2004), Observations of common microstructural issues associated with dynamic deformation phenomena: Twins, microbands, grain size effects, shear bands, and dynamic recrystallization, *J. Mater. Sci.*, *39*(4), 1153–1168, doi:10.1023/B:JMSC.0000013870.09241.c0.

Muxworthy, A. R., and D. J. Dunlop (2002), First-order reversal curve (FORC) diagrams for pseudo-single-domain magnetites at igh temperature, *Earth Planet. Sci. Lett.*, *203*(1), 369–382, doi:10.1016/S0012-821X(02)00880-4.

Muxworthy, A. R., D. J. Dunlop, and Ö. Özdemir (2003), Low-temperature cycling of isothermal and anhysteretic remanence: Microcoercivity and magnetic memory, *Earth Planet. Sci. Lett.*, *205*(3-4), 173–184, doi:10.1016/S0012-821X(02)01039-7.

Nagata, T., and H. Kinoshita (1964), Effect of release of compression on magnetization of rocks and assemblies of magnetic minerals, *Nature*, *204*(4964), 1183–1184, doi:10.1038/2041183a0.

Olsen, J. S., L. Gerward, E. Hinze, and J. Kremmler (1994), High-pressure, high-temperature study of magnetite using synchrotron radiation, *Mater. Sci. Forum*, *166-169*, 577–582, doi:10.4028/www.scientific.net/MSF.166-169.577.

Özdemir, Ö., and D. J. Dunlop (1999), Low-temperature properties of a single crystal of magnetite oriented along principal magnetic axes, *Earth Planet. Sci. Lett.*, *165*(2), 229–239, doi:10.1016/S0012-821X(98)00269-6.

Pesonen, L. J., A. Deutsch, U. Hornemann, and F. Langenhorst (1997), Magnetic properties of diabase samples shocked experimentally in the 4.5 to 35 GPa range, *Lunar Planet. Sci.* [CD-ROM], *XXVIII*, Abstract 1370.

Pike, C. (2003), First-order reversal-curve diagrams and reversible magnetization, *Phys. Rev. B*, *68*(10), 1–5, doi:10.1103/PhysRevB.68.104424.

Prabhu, Y. T., and K. V. Rao (2014), X-Ray analysis by williamson-hall and size-strain plot methods of zno nanoparticles with fuel variation, *World J. Nano Sci. Eng.*, *4*, 21–28, doi:10.4236/wjnse.2014.41004.

Rasband, W. S. (1997), ImageJ and U. S. National Institutes of Health, Bethesda, Md. [Available at http://imagej.nih.gov/ij/.]

Rochette, P., J. P. Lorand, G. Fillion, and V. Sautter (2001), Pyrrhotite and the remanent magnetization of SNC meteorites: A changing perspective on Martian magnetism, *Earth Planet. Sci. Lett.*, *190*(1-2), 1–12, doi:10.1016/S0012-821X(01)00373-9.

Rozenberg, G., M. Pasternak, W. Xu, Y. Amiel, M. Hanfland, M. Amboage, R. Taylor, and R. Jeanloz (2006), Origin of the verwey transition in magnetite, *Phys. Rev. Lett.*, *96*(4), 045705, doi:10.1103/PhysRevLett.96.045705.

RusBank. [Available at http://teos.ficp.ac.ru/rusbank/.]

Schäffer, H., W. F. Mfiller, U. Hornemann, I. Mineralogie, T. H. Darmstadt, and W. Germany (1983), Shock Effects in MgAl204-Spinel, *Phys. Chem. Miner.*, *4*, 248–252.

Thapa, D., V. R. Palkar, M. B. Kurup, and S. K. Malik (2004), Properties of magnetite nanoparticles synthesized through a novel chemical route, *Mater. Lett.*, *58*(21), 2692–2694, doi:10.1016/j.matlet.2004.03.045.

Tikoo, S. M., J. Gattacceca, N. L. Swanson-Hysell, B. P. Weiss, C. Suavet, and C. Cournède (2015), Preservation and detectability of shock-induced magnetization, *J. Geophys. Res. Planets*, *120*, 1461–1475, doi:10.1002/2015JE004840.

Todo, S., N. Takeshita, T. Kanehara, T. Mori, and N. Môri (2001), Metallization of magnetite (Fe3O4) under high pressure, *J. Appl. Phys.*, *89*(11), 7347–7349, doi:10.1063/1.1359460.

Ugalde, H. A., N. A. Artemieva, and B. Milkereit (2005), Magnetization on impact structures; constraints from numerical modeling and petrophysics, *Spec. Pap. Geol. Soc. Am.*, *384*, 25–42, doi:10.1130/0-8137-2384-1.25.

Williams, W., and D. J. Dunlop (1995), Simulation of magnetic hysteresis in pseudo-single-domain grains of magnetite, *J. Geophys. Res.*, *100*(B3), 3859–3871.

Williamson, G. K., and W. H. Hall (1953), Williamson and Hall—X-ray line broadening from filed aluminum and wolfram, *Acta Metall.*, *1*(1), 22–31.